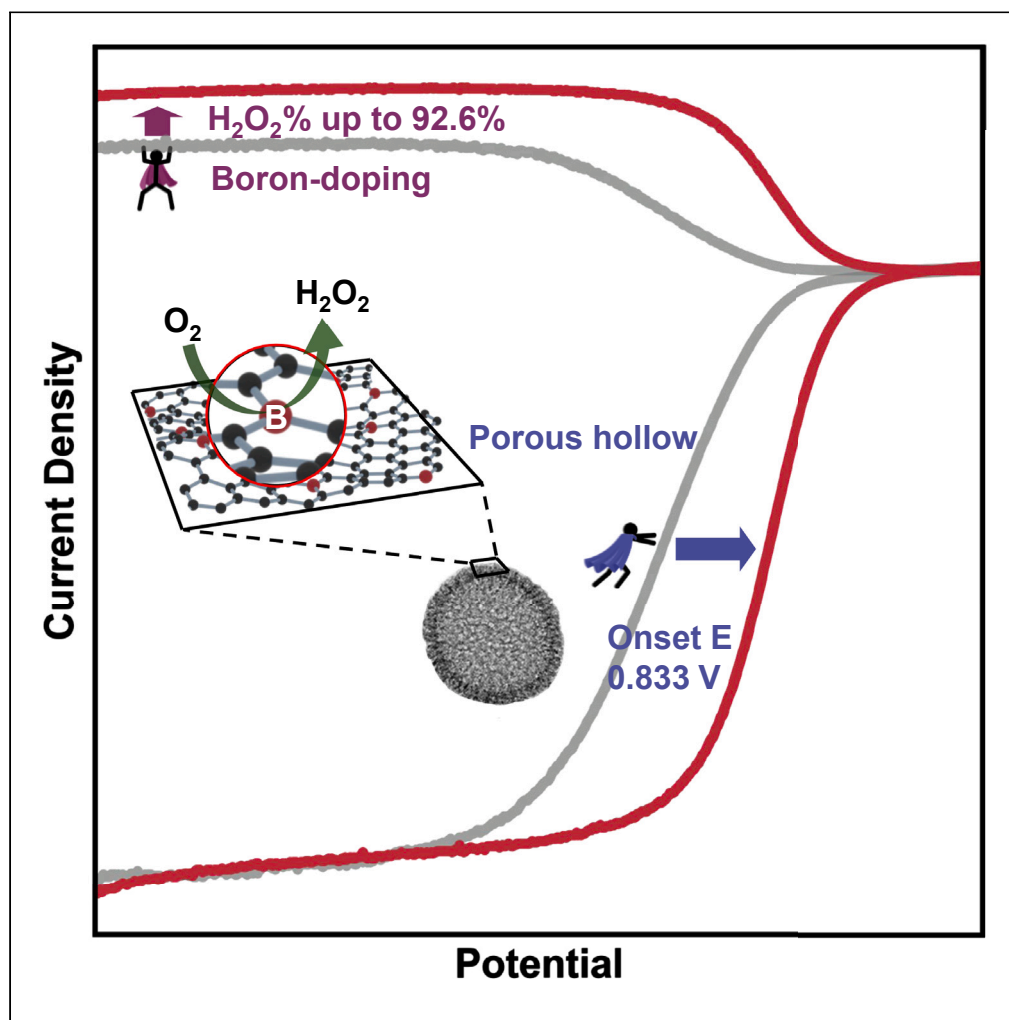


## Article

Enhanced electrocatalytic performance for  $\text{H}_2\text{O}_2$  generation by boron-doped porous carbon hollow spheres

Zhaohui Wang,  
Zehan Sun, Kun Li,  
..., Yanzhi Sun,  
Pingyu Wan,  
Yongmei Chen

chenym@buct.edu.cn

**Highlights**

$\text{SiO}_2$  hard template  
coupled with borate  
transesterification

B doping:  $\text{H}_2\text{O}_2\%$  > 90% at  
0.4–0.7 V

Porous hollow  
morphology:  $E_{\text{onset}}$  of  
0.833 V

Wang et al., iScience 27,  
109553  
April 19, 2024 © 2024 The  
Authors. Published by Elsevier  
Inc.  
[https://doi.org/10.1016/  
j.isci.2024.109553](https://doi.org/10.1016/j.isci.2024.109553)

## Article

Enhanced electrocatalytic performance for H<sub>2</sub>O<sub>2</sub> generation by boron-doped porous carbon hollow spheresZhaohui Wang,<sup>1,4</sup> Zehan Sun,<sup>1,2,4</sup> Kun Li,<sup>1</sup> Keyi Fan,<sup>1</sup> Tian Tian,<sup>1</sup> Haomin Jiang,<sup>3</sup> Honglei Jin,<sup>1</sup> Ang Li,<sup>1</sup> Yang Tang,<sup>1</sup> Yanzhi Sun,<sup>1</sup> Pingyu Wan,<sup>1</sup> and Yongmei Chen<sup>1,5,\*</sup>

## SUMMARY

Electrocatalytic generation of H<sub>2</sub>O<sub>2</sub> via the 2-electron pathway of oxygen reduction reaction (2e-ORR) is an attractive technology compared to the anthraquinone process due to convenience and environmental friendliness. However, catalysts with excellent selectivity and high activity for 2e-ORR are necessary for practical applications. Reported here is a catalyst comprising boron-doped porous carbon hollow spheres (B-PCHSs) prepared using the hard template method coupled with borate transesterification. In an alkali electrolyte, the selectivity of B-PCHS for 2e-ORR above 90% in range of 0.4–0.7 V<sub>RHE</sub> and an onset potential of 0.833 V was obtained. Meanwhile, the generation rate of H<sub>2</sub>O<sub>2</sub> reached 902.48 mmol h<sup>-1</sup> g<sub>cat</sub><sup>-1</sup> at 0.4 V<sub>RHE</sub> under 59.13 mA cm<sup>-2</sup> in batch electrolysis. The excellent catalytic selectivity of B-PCHS for 2e-ORR originates from the boron element, and the catalytic activity of B-PCHS for H<sub>2</sub>O<sub>2</sub> generation is contributed to the morphology of porous hollow spheres, which facilitates mass transfer processes.

## INTRODUCTION

Hydrogen peroxide (H<sub>2</sub>O<sub>2</sub>) is a sustainable and environmentally friendly oxidizing agent extensively utilized in clinical disinfection, wastewater treatment, fine chemical synthesis, energy storage, and other applications.<sup>1</sup> Currently, the industrial manufacturing of H<sub>2</sub>O<sub>2</sub> is predominantly carried out through the anthraquinone process, resulting in the production of up to 75 wt % concentrated H<sub>2</sub>O<sub>2</sub> solution, but commercially available in 27–30 wt % to balance costs and mitigate risks associated with storage and transportation.<sup>2</sup> However, a 3 wt % of H<sub>2</sub>O<sub>2</sub> solution is sufficient for clinical sterilization, highlighting the potential for an electrochemical method to prepare H<sub>2</sub>O<sub>2</sub> on demand in these settings.<sup>3</sup>

Electrocatalytic generation of H<sub>2</sub>O<sub>2</sub> can be achieved through the two-electron pathway of the reduction reaction of O<sub>2</sub> (2e-ORR) on the cathode. Nevertheless, the competitive reaction on the cathode is the process of O<sub>2</sub> reduction to H<sub>2</sub>O/OH<sup>-</sup>, known as the four-electron pathway of oxygen reduction reaction (4e-ORR), and it is more thermodynamically favorable than 2e-ORR.<sup>4</sup> Researchers have discovered that the selectivity of the ORR pathways is dependent on the adsorption mode of O<sub>2</sub> molecules on the cathodic catalysts. The O<sub>2</sub> molecules adsorbed on the catalyst in the end-on form (Pauling model) are more likely to undergo the 2e-ORR pathway with the associated reaction mechanism than those adsorbed in the bridge form.<sup>5,6</sup> Moreover, the adsorption strength of the transient state of \*OOH on the catalyst also affects the selectivity of ORR pathways.<sup>7</sup> A relationship resembling a volcano shape has been proposed between the catalytic activity for 2e-ORR and the value of the adsorption-free energy of \*OOH (ΔG<sub>OOH\*</sub>). This suggests that a catalyst with an appropriate value of ΔG<sub>OOH\*</sub> (near the peak of the volcano) is desired for H<sub>2</sub>O<sub>2</sub> generation: a catalyst with a lower value is unfavorable for initial O<sub>2</sub> adsorption, while one with a higher value is unfavorable for \*OOH release, resulting in further reduction.<sup>8,9</sup>

Various types of promising catalysts for 2e-ORR have been reported, such as noble metal-based catalysts (Pd-Hg<sup>10</sup>), non-noble metal catalysts (Co-N<sub>4</sub>-C,<sup>11,12</sup> Sb<sub>2</sub>S<sub>3</sub>,<sup>13</sup> SnO<sub>2</sub>,<sup>14</sup> metal-organic framework (MOF),<sup>15</sup> etc.), and a range of carbon-based materials. Among these materials, carbon-based materials are the most attractive due to their affordability, abundance, and excellent electrical conductivity. Numerous studies have confirmed that O<sub>2</sub> molecules tend to adsorb in an end-on mode on carbon-based catalysts.<sup>16</sup> To enhance the catalytic activity, researchers have experimented with doping carbon materials with various elements, including O, N, S, and others.<sup>17–20</sup> The corresponding theoretical calculations indicate that, when sp<sup>2</sup>-hybridized carbon is doped with non-metallic elements, O<sub>2</sub> molecules tend to adsorb on the carbon atoms adjacent to the heteroatoms in an end-on manner, leading to a relatively high adsorption energy of \*OOH.<sup>21</sup>

<sup>1</sup>Institute of Applied Electrochemistry, College of Chemistry, Beijing University of Chemical Technology, Beijing 100029, P.R. China

<sup>2</sup>State Key Laboratory of Fine Chemicals, School of Chemistry, Dalian University of Technology, Dalian 116024, P.R. China

<sup>3</sup>Center for Advanced Materials Research, College of Chemistry, Beijing Normal University, Zhuhai 519087, P.R. China

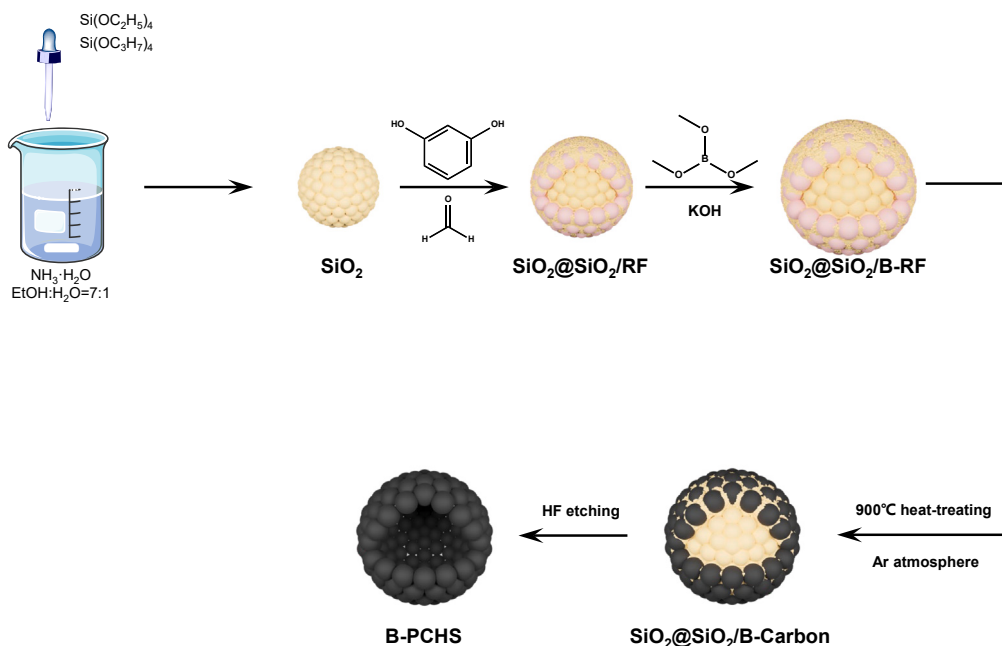
<sup>4</sup>These authors contributed equally

<sup>5</sup>Lead contact

\*Correspondence: chenym@buct.edu.cn

<https://doi.org/10.1016/j.isci.2024.109553>





**Scheme 1. Schematic diagram of B-PCHS preparation**

Xia's group discovered that boron-doped (B-doped) carbon catalysts demonstrate better performance for 2e-ORR compared to carbon doped by other elements, as evidenced by both theoretical and experimental studies. The results revealed that  $\text{O}_2$  molecules have a tendency to directly adsorb onto the boron atoms in B-doped carbon material, leading to a lower adsorption energy of  $^*\text{OOH}$ , bringing it closer to the peak of the volcano curve.<sup>17</sup> Building on this concept, various types of B-doped carbon catalysts have been examined, and the findings indicate that a moderate amount of doped boron atoms can significantly improve the 2e-ORR selectivity of carbon materials, while excessive boron doping may diminish the catalytic activity due to disruption of the graphitized structure of the carbon materials caused by the boron doping.<sup>22–25</sup>

However, heteroatom-doped carbon materials have been reported to have unsatisfactory ORR catalytic activity, despite their excellent selectivity due to weak  $^*\text{OOH}$  binding.<sup>9,22</sup> For the electrocatalytic production of  $\text{H}_2\text{O}_2$ , high selectivity must be achieved alongside relatively high activity to be practically significant. To reconcile the conflicting limitations on the activity and selectivity of B-doped carbon catalyst for 2e-ORR, we prepared a type of boron-doped porous carbon hollow sphere (B-PCHS) and utilized it as an electrocatalyst for  $\text{H}_2\text{O}_2$  generation. In previous studies, porous carbon hollow spheres (PCHSs) have been prepared using  $\text{SiO}_2$  as the hard template and phenolic resin as the precursor<sup>26</sup> and applied as special adsorbents, supercapacitor electrodes, and catalyst carriers due to their regular morphology and large specific surface area.<sup>27,28</sup> Pang et al. pioneered the use of PCHS in the 2e-ORR direction, but it only exhibited promising catalytic selectivity in a weakly alkaline electrolyte.<sup>29</sup> In this study, B atoms were managed to be introduced into the carbon skeleton through transesterification during the preparation of PCHS. As anticipated, the acquired B-PCHS exhibited excellent catalytic activity and selectivity, as well as a long-term stability for  $\text{H}_2\text{O}_2$  generation in an alkaline electrolyte solution.

## RESULTS AND DISCUSSION

### Preparation and characterization

The structure of porous hollow spheres in B-PCHS was created by applying a phenolic resin onto two types of  $\text{SiO}_2$  particles with different sizes as hard templates,<sup>29</sup> while the introduction of the B element was achieved through borate transesterification during the formation of the phenolic resin. The schematic diagram for the preparation of B-PCHS is shown in Scheme 1. Two silicates, tetraethyl silicate (TEOS) and tetrapropyl silicate (TPOS), were used as silicon sources, and their hydrolysis reaction rates were different. This allowed for the assembly of the formed  $\text{SiO}_2$  particles to be designed to construct an elaborate secondary structure. The hydrolysis rate of TEOS was faster, leading to the formation of  $\text{SiO}_2$  particles with a larger size (more than 100 nm) that aggregated with each other under stirring. While the hydrolysis rate of TPOS was slightly slower, the formed  $\text{SiO}_2$  particles (in their primary nanoparticles 5–10 nm) and the particles of resorcinol formaldehyde (RF) resin, formed by subsequently added resorcinol and formaldehyde, assembled onto the surface of the  $\text{SiO}_2$  core through hydrogen bonding. This resulted in the formation of a shell-core structure, with a shell composed of small-sized  $\text{SiO}_2$  particles and RF particles, and a core consisting of large-sized  $\text{SiO}_2$  spheres.<sup>26</sup> After carbonization and HF etching, the desired structure of porous hollow carbon spheres was obtained.

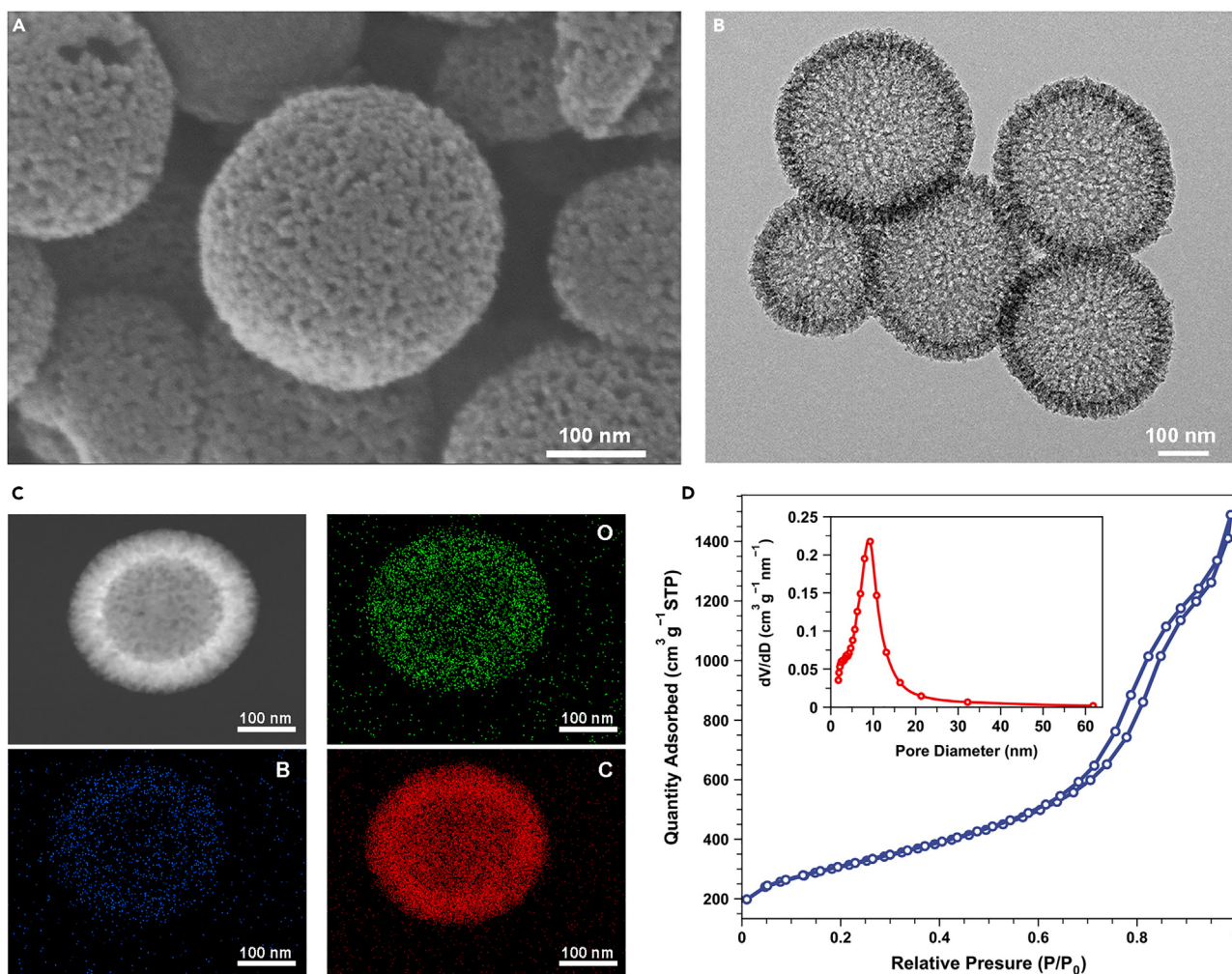


**Figure 1. The morphology of the synthesized catalysts**

(A and B) SEM (A) and TEM (B) images of B-PCHS and PCHS.

(C) TEM-EDS O, B, and C color-mapping images of B-PCHS.

(D) N<sub>2</sub> adsorption-desorption isotherm of B-PCHS and the average pore size plot (inset image).

During the preparation of B-PCHS, a borate ester solution containing H<sub>3</sub>BO<sub>3</sub> and CH<sub>3</sub>OH was added to the reaction system along with resorcinol and formaldehyde. As a result, some of the phenolic hydroxyl groups in RF particles were replaced by -OB(OCH<sub>3</sub>)<sub>2</sub> groups through transesterification.<sup>30</sup> Subsequently, B atoms were introduced into the B-PCHS after carbonization and etching.

The sample without boron doping, denoted as PCHS, was also prepared as a reference. In addition, another sample (denoted as pre-B-PCHS) synthesized directly from boron-doped resorcinol was used for comparison in this study. The preparation procedure of the aforementioned two comparison samples was also described in Scheme 1.

The scanning electron microscopy (SEM) image of the final B-PCHS (Figure 1A) reveals well-dispersed spheres with diameters of 200–300 nm and numerous surface pores. The transmission electron microscopy (TEM) image (Figure 1B) reveals that these porous spheres are hollow, with a shell thickness of about 30 nm and channels penetrating through the shell. In addition, the energy dispersive spectrometer (EDS) mapping images (Figure 1C) reveal that C, O, and B elements are evenly distributed in the shell of B-PCHS. Compared with the images of the non-doping PCHS (shown in Figure S1), the pore size in PCHS is significantly smaller than that of B-PCHS, and the shell in PCHS is thicker than that of B-PCHS. The alterations in the fine structure of porous spheres are likely caused by the influence of borate transesterification during the formation of these porous spheres. The impact of doped boron atoms was hypothesized in two aspects. One is that the charge density on C<sub>β</sub> atoms of resorcinol decreased after the -OH groups on the adjacent C atoms were transformed into -OB(OCH<sub>3</sub>)<sub>2</sub> groups. The transformation caused the polycondensation reaction to slow down because the C<sub>β</sub> atoms act as the nucleophilic centers in RF polycondensation. The other is that the strength of hydrogen bonds between the O atoms in the B-doped RF and SiO<sub>2</sub> particles is weakened due to the electron-pulling effect of the adjacent boron atoms, resulting in poor coverage of RF on the surface

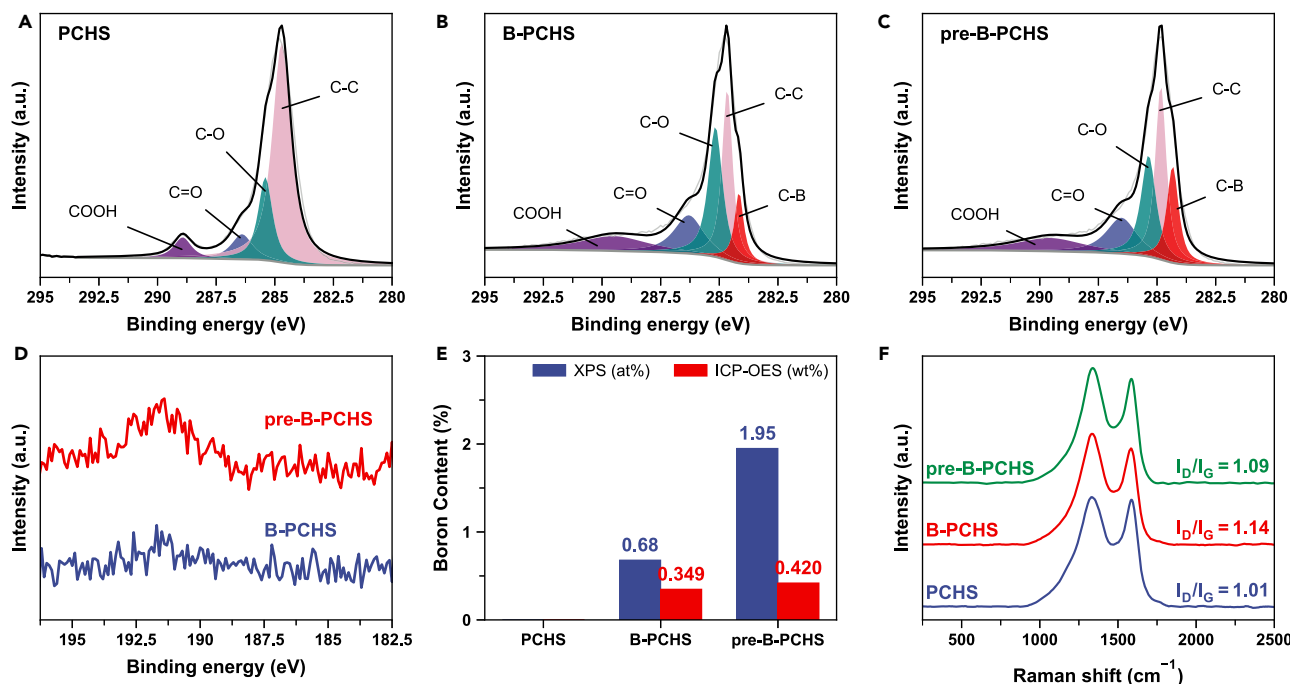


**Figure 2. The compositional characterization of synthesized catalysts**

(A–C) XPS C1s spectra of (A) B-PCHS, (B) pre-B-PCHS, and (C) PCHS.

(D) XPS B1s spectra of B-PCHS and pre-B-PCHS.

(E) B contents obtained from XPS and ICP-OES in different catalysts.

(F) Raman spectra of different catalysts.

of SiO<sub>2</sub> particles. The mismatch in the polycondensation rate of RF particles with the formation rate of SiO<sub>2</sub> particles, along with inadequate coverage, led to the formation of more SiO<sub>2</sub> particles and fewer RF particles in the shell. This resulted in a shell with larger-sized pores and a thinner thickness in B-PCHS.

The morphology of the comparison sample (pre-B-PCHS) might serve as indirect evidence for the aforementioned explanation. The morphology of the pre-B-PCHS sample resembles deflated spheres that are adhered to each other (Figure S2). The deflated and adhered spheres may be caused by the shell thickness being too thin. The use of B-doped resorcinol in the preparation of pre-B-PCHS resulted in a lower reaction rate of RF. Additionally, the hydrogen bonding between the B-doped RF particles and the SiO<sub>2</sub> particles was weakened, leading to the formation of a thinner shell in pre-B-PCHS compared to B-PCHS.

It is not surprising that B-PCHS has an exceptionally high specific surface area of 1070.10 m<sup>2</sup> g<sup>-1</sup>. Its adsorption and desorption curves (Figure 1D) exhibited an H3-type hysteresis loop and were classified as type IV isotherm, indicating the occurrence of capillary coalescence phenomenon during N<sub>2</sub> adsorption and desorption. This suggests the presence of a fine secondary porous structure in B-PCHS. Furthermore, the average pore size of B-PCHS was calculated as 9.21 nm based on the Barret-Joyner-Halenda (BJH) pore size distribution from the desorption curve portion (Figure 1D, inset), which is larger than that of non-doping PCHS (5.70 nm). The architecture of porous hollow spheres in an electrocatalyst is reported to be beneficial for the electrode kinetics of the ORR process since it is a typical diffusion-controlled reaction in which mass transfer is crucial to the reaction rate.<sup>31</sup> Furthermore, hollow spheres with meso-sized pores exhibit greater stability in catalytic performance for ORR compared to those with micro-sized pores, because the mesoporous structure keeps the active sites dispersed, avoiding their deactivation.<sup>30,31</sup>

The X-ray photoelectron spectroscopy (XPS) spectra of PCHS, B-PCHS, and pre-B-PCHS are shown in Figures 2A–2D. A deconvoluted peak centered at 284.1 eV was observed in the C1s spectra of both B-PCHS (Figure 2B) and pre-B-PCHS (Figure 2C), while it is absent from that of PCHS (Figure 2A). It is reasonable to assign this peak to the C-B bond. Correspondingly, faint peaks around 192 eV were observed in the B1s spectra of B-PCHS and pre-B-PCHS (Figure 2D), but not in the spectrum of PCHS (Figure S3). The B contents in these samples were estimated semi-quantitatively according to the XPS results, and the precise contents were determined by the inductively coupled plasma-optical emission spectrometry (ICP-OES) method. As shown in Figure 2E, the B content in pre-B-PCHS is higher than that of B-PCHS, which is contributed to the variance in the preparation procedure.

The Raman spectra of PCHS, pre-B-PCHS, and B-PCHS are shown in Figure 2F, in which the D band at 1,350 cm<sup>-1</sup> and the G band at 1,580 cm<sup>-1</sup> correspond to the disordered C-C bonds and the graphitized (sp<sup>2</sup> hybridized) C-C bonds, respectively. The intensity ratio of D and G bands ( $I_D/I_G$ ) indicates the degree of graphitization in the carbon materials.<sup>32</sup> The results show that the  $I_D/I_G$  ratios of PCHS,

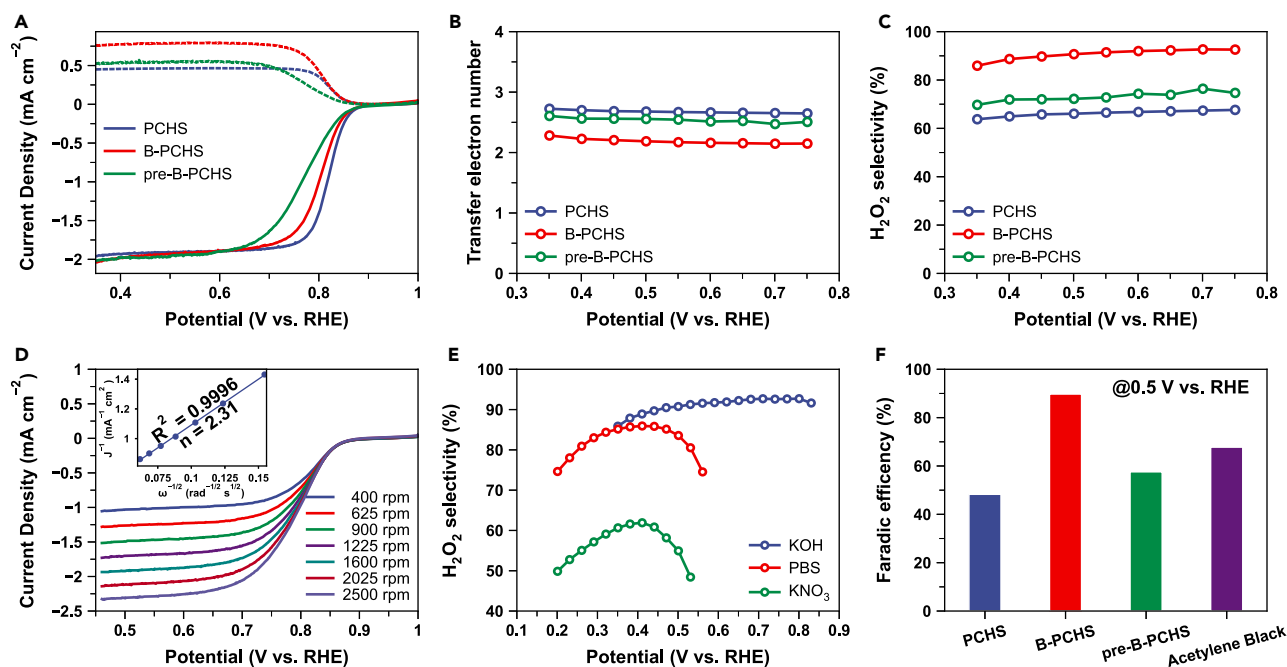


**Figure 3. The 2e-ORR selectivity of the synthesized catalysts**

(A) The RRDE voltammograms of catalysts at 1,600 rpm in  $O_2$ -saturated  $1 \text{ mol L}^{-1}$  KOH electrolyte. the transfer electron numbers (B), and the  $H_2O_2$  selectivity (C) of different catalysts.

(D) The LSV curves of B-PCHS at increasing rotating speeds and K-L plot (insert) at half-wave potential (0.79 V).

(E) Calculated  $H_2O_2$  selectivity of PCHS in different electrolytes.

(F) FEs for  $H_2O_2$  of different catalysts obtained by the chronoamperometry tests in  $1 \text{ mol L}^{-1}$  KOH at 0.5 V.

pre-B-PCHS, and B-PCHS are 1.01, 1.09, and 1.14, respectively. This finding suggests that the graphitization structure in B-PCHS is inferior to that in PCHS and pre-PCHS, possibly due to the incorporation of B atoms into the graphite structure.

### Catalytic selectivity for 2e-ORR

The cathodic peak observed at 0.78 V in the cyclic voltammetry (CV) curve of the B-PCHS-loaded electrode in a  $1 \text{ mol L}^{-1}$  KOH solution under  $O_2$  atmosphere (Figure S4) originates from the 2e reduction pathway of  $O_2$  on the cathode, implying the catalytic ability of B-PCHS for the 2e-ORR process. To assess the impact of boron doping on the intrinsic 2e-ORR catalytic performance, rotating ring-disk electrode (RRDE) measurements of PCHS, B-PCHS, and pre-B-PCHS were compared, as depicted in Figure 3A. Recognized from its highest ring currents, B-PCHS demonstrated the highest selectivity for  $H_2O_2$  generation. The transferred electron numbers ( $n$ ) during the catalyzed ORR process, calculated based on the ring currents and disk currents of RRDE tests, are shown in Figure 3B. The result of  $n \approx 2.15$  for B-PCHS implies a satisfied 2e-ORR selectivity.

The calculation results for the  $H_2O_2$  selectivity of these three catalysts, based on the linear sweep voltammetry (LSV) curves, are shown in Figure 3C. B-PCHS demonstrated catalytic activity for 2e-ORR with a selectivity above 90% across the entire testing potential range of 0.45–0.75  $V_{RHE}$  and achieve the highest selectivity of 92.7% at 0.68  $V_{RHE}$ . Meanwhile, the selectivity of pre-B-PCHS and non-doping PCHS is 70%–75% and 64%–68%, respectively, in the testing potential range. To further confirm this result, the LSV curves at different rotating rates (Figure 3D) were conducted. Based on the currents at 0.79 V, the value  $n$  for B-PCHS was calculated as 2.31 using the Koutechy-Levich equation (inset of Figure 3D). The consistency of the results obtained by RRDE and the K-L equation demonstrates the accuracy of the experimental findings.

By using the catalyst-loaded electrode as cathodes in an H-type bath with a  $1 \text{ mol L}^{-1}$  KOH solution, the catalytic performance was evaluated based on the amount of  $H_2O_2$  generated in the electrolyte after the electrolysis at a constant potential of 0.5 V for 1,200 s. As shown in Figure 3F, the Faradaic efficiency (FE) of  $H_2O_2$  generation over PCHS, B-PCHS, and pre-B-PCHS is 48.3%, 89.8%, and 57.6%, respectively. The sequence aligns with the selectivity results measured through the RRDE and LSV methods, confirming the superior performance of B-PCHS for 2e-ORR compared to PCHS and pre-B-PCHS.

The excellent catalytic selectivity of B-PCHS for  $H_2O_2$  generation is likely due to the appropriate doping amount of boron atoms. In further experiments, a series of B-PCHS samples with varying B density were synthesized (Figure S5). The synthesis procedure has remained almost the same as that of B-PCHS, with the exception of the amounts of  $H_3BO_3$  and methanol added (see supplemental information for more details). The concentrations of B atoms range from 0.140% to 0.414% as determined by the ICP-OES method. Assessed by RRDE, the  $H_2O_2$

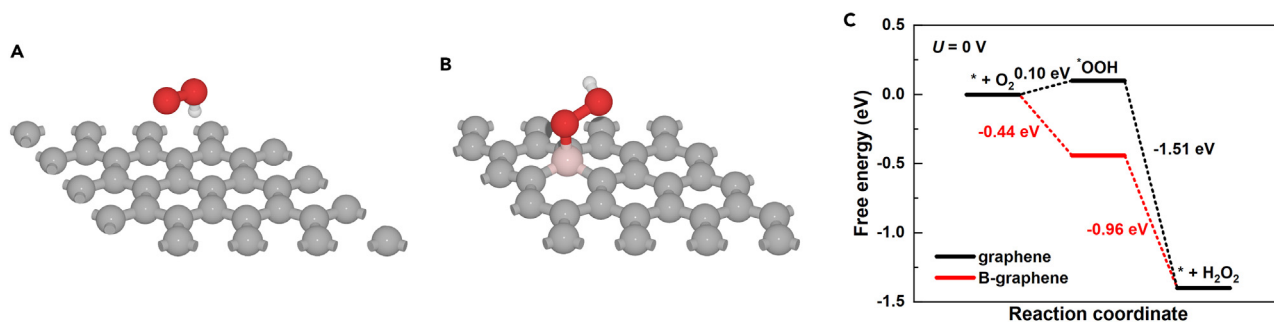


**Figure 4. DFT calculations**

(A and B) Optimized structures of \*OOH on bare graphene (A) and B-doped graphene (B).  
(C) The free energy diagram of 2e-ORR process on bare graphene and B-doped graphene.

selectivity increased as the concentration of B increased, reaching a maximum of 93% at a B content of 0.360% and then decreased when the B content reached 0.414%.

The role of doped B atoms was revealed by density functional theory (DFT) calculations. From the free energy diagram of the 2e-ORR process (Figure 4C), the potential-determination step of graphene with or without B doping is recognized as the adsorption of oxygen molecule to the catalyst surface to form \*OOH. There is almost no interaction between OOH and the bare graphene surface (Figure 4A), resulting in oxygen adsorption only occurring at  $-0.1$  V. As for the B-doped graphene, OOH can form chemical bond with B atom (Figure 4B), and oxygen can be adsorbed at a potential as high as 0.44 V.

The impact of the pH value of the electrolyte on the 2e-ORR selectivity of B-PCHS was investigated using identical testing conditions in  $1 \text{ mol L}^{-1}$  phosphate-buffered saline (PBS, pH = 8) and  $1 \text{ mol L}^{-1}$   $\text{KNO}_3$  solution. As shown in Figure 3E, a selectivity of 70%–85% is achieved in PBS, whereas, in a neutral  $\text{KNO}_3$  solution, the selectivity is only 45.6%–62.0%. This result is consistent with the reported findings that the doped B atoms offer superior catalytic performance for the 2e-ORR in an alkaline electrolyte compared to other electrolytes.<sup>17,23</sup>

### Catalytic activity for 2e-ORR

The term of “catalytic activity for 2e-ORR” is commonly used to describe the kinetic characteristics of the catalyzed 2e-ORR reaction, and “a higher catalytic activity” indicates that  $\text{H}_2\text{O}_2$  could be generated at a more positive potential (less overpotential for the ORR process) with a larger current intensity (faster generation rate).<sup>25</sup> The catalytic activity for 2e-ORR is typically evaluated by the onset potential of the ring current in RRDE tests or by electrochemical methods like Tafel and electrochemical impedance spectroscopy (EIS) measurement.

The onset potentials at which the corresponding ring current density reaches  $0.15 \text{ mA cm}^{-2}$  and the corresponding half-wave potentials ( $E_{1/2}$ ) of these catalysts are listed in Figure 5A. The onset potentials of B-PCHS (0.833 V) and PCHS (0.832 V) are more positive than the potential of pre-B-PCHS (0.804 V). It should be mentioned that the electrolyte used in this work was  $1 \text{ mol L}^{-1}$  KOH, in which the measured value of onset potential is more positive than that in  $0.1 \text{ mol L}^{-1}$  KOH; for example, the onset potential of B-PCHS in a  $0.1 \text{ mol L}^{-1}$  KOH solution is 0.804 V (see the details in Figure S6). Compared to the values of the onset potentials of the recently reported catalysts (Figure 5C), B-PCHS and PCHS in this study might be listed in the most active catalysts for 2e-ORR in alkali electrolytes.<sup>9,13,17,24,32–37</sup>

As mentioned earlier, both PCHS and B-PCHS exhibit better morphology of porous hollow spheres than pre-B-PCHS. This type of morphology appears to benefit mass transfer in the 2e-ORR process which is a diffusion-controlled process. The following electrochemical studies confirmed the speculation. As shown in Figure 5B, the Tafel slopes calculated using the staircase voltammetry method (SCV) are  $38.2 \text{ mV dec}^{-1}$  for PCHS and  $40.9 \text{ mV dec}^{-1}$  for B-PCHS, which are lower than the Tafel slope of pre-B-PCHS ( $47.8 \text{ mV dec}^{-1}$ ). The double-layer capacitances ( $C_{dl}$ ) of the catalysts were calculated from CV results under Ar atmosphere (Figure S7). As shown in Figure 5D, PCHS and B-PCHS demonstrated a higher  $C_{dl}$  of  $2.81 \text{ mF cm}^{-2}$  compared to that of pre-B-PCHS ( $2.04 \text{ mF cm}^{-2}$ ). More importantly, the calculated  $C_{dl}$  of pre-B-PCHS at a higher scan rate of  $400 \text{ mV s}^{-1}$  was only 24% of that at  $100 \text{ mV s}^{-1}$ , while PCHS and B-PCHS reached 75.5% and 59.4%, respectively. It is commonly believed that higher  $C_{dl}$  retention at a high scan rate indicates higher rate capability for mass transfer.<sup>38</sup> Finally, the EIS was conducted at the respective half-wave potentials of the catalysts in  $\text{O}_2$  atmosphere with the electrode rotating at 1,600 rpm (see details in supplemental information), and the diffusion resistance  $R_d$  of PCHS, B-PCHS, and pre-B-PCHS was fitted as 181, 521, and  $1347 \Omega$ , respectively. All these results indicate that the morphology of porous carbon hollow spheres in PCHS and B-PCHS is beneficial for mass transfer during the ORR process, which is the main factor contributing to the excellent catalytic activity of ORR.

The results of the continuous electrolysis catalyzed by B-PCHS in a bath are shown in Figure 5D; the FE remains above 85% when the cathodic potential was maintained within the range of 0.4–0.7 V. At 0.4 V, the generation rate of  $\text{H}_2\text{O}_2$  reached  $902.48 \text{ mmol h}^{-1} \text{ g}_{\text{cat}}^{-1}$  with a current density of  $59.13 \text{ mA cm}^{-2}$ . Achieving a higher generation rate of  $\text{H}_2\text{O}_2$  with less overpotential means lower bath voltage is required during the electrolysis process. This could be the key point for power saving, as several electrode processes, including the oxygen evolution reaction (OER), two-electron water oxidation reaction (2e-WOR), and the urea oxidation reaction (UOR) might occur simultaneously on the anode in an aqueous electrolyte.

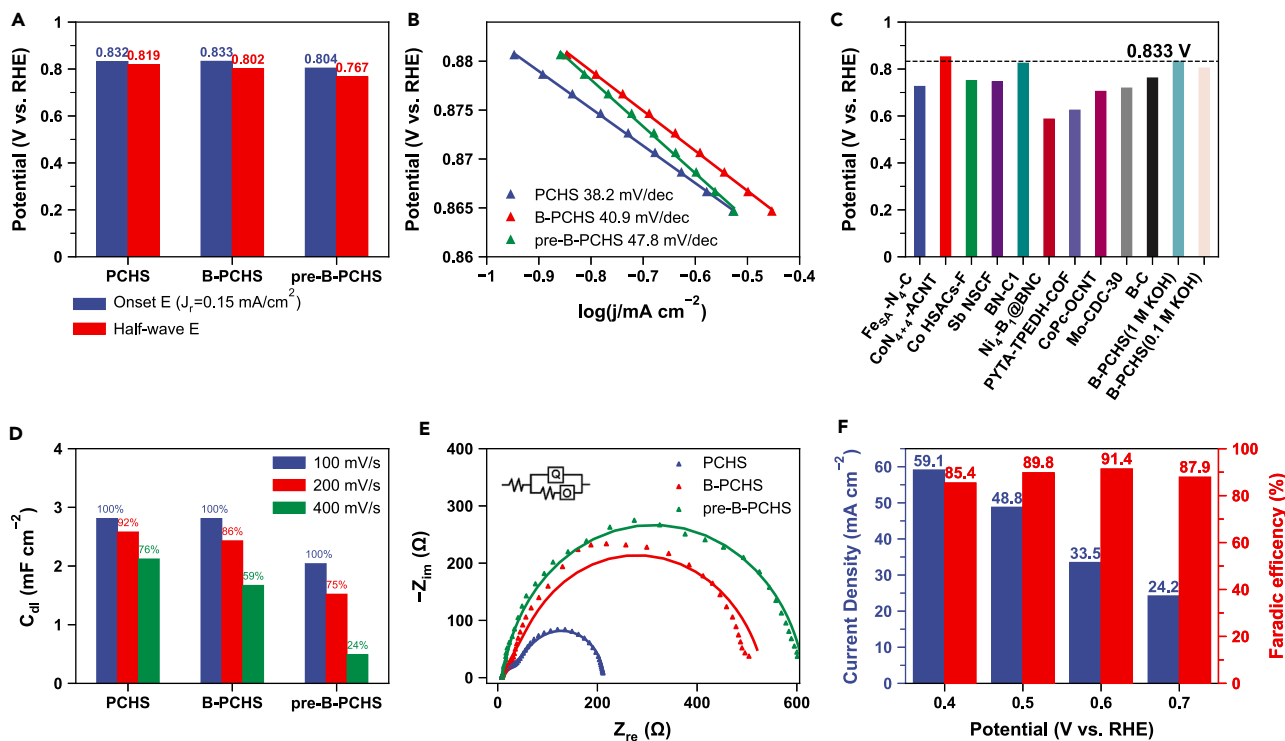


**Figure 5. The catalytic activity of the synthesized catalysts**

- (A) The onset potential and half-wave potential of each catalyst.  
 (B) The Tafel plots of different catalysts.  
 (C) The comparison of ring onset potential to that of reported electrocatalysts in the alkaline electrolytes.  
 (D) The double-layer capacitances at different potential scan rates.  
 (E) The electrochemical impedance spectroscopy of different catalysts.  
 (F) Faraday efficiency and current density of B-PCHS at different potentials.

### Stability

The stability of the B-PCHS itself and its catalytic activity were tested by several methods. To determine if the formed H<sub>2</sub>O<sub>2</sub> could deactivate the catalyst, the LSV curves of the loaded electrode were measured before and after soaking B-PCHS in a 0.1 mol L<sup>-1</sup> H<sub>2</sub>O<sub>2</sub>/1 mol L<sup>-1</sup> KOH solution for 48 h. Only little changes in the LSV curves (Figure S8) demonstrated the chemical stability of B-PCHS. The chronoamperometry test was performed using an RRDE with B-PCHS loaded on the disk electrode, and the potential was kept constant at 0.5 V for 20 h. As shown in Figure 6A, the current recorded on the ring electrode did not exhibit a significant decay trend. The stability of B-PCHS's catalytic activity was also tested through an accelerated durability test (ADT) in oxygen-saturated 1 mol L<sup>-1</sup> KOH. As shown in Figure S9, the difference between

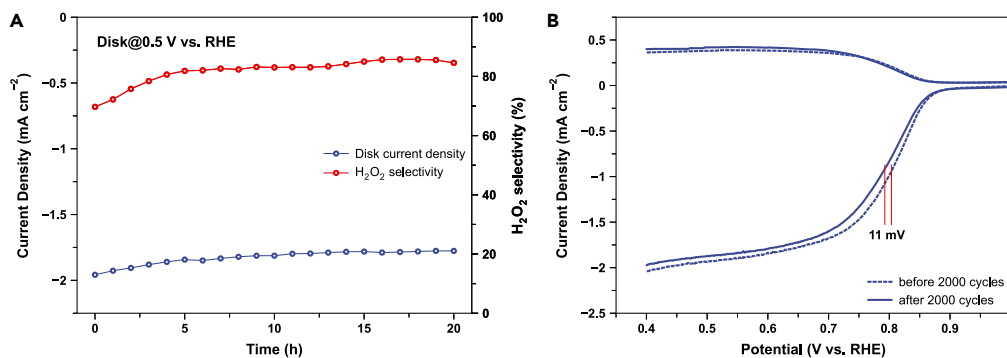


**Figure 6. The stability test of B-PCHS**

- (A) Disk current density and H<sub>2</sub>O<sub>2</sub> selectivity during chronoamperometry for 20 h, with a disk potential of 0.5 V and a ring potential of 1.2 V.  
 (B) LSV curves before and after 2,000 ADT cycles in the potential range of 0.2–1.0 V under O<sub>2</sub>.

the CV curves before and after 2,000 cycles is indistinct. When comparing the LSV curves before and after the ADT test (Figure 6B), the decrease in half-wave potential is approximately 11 mV, and the reduction in catalytic activity is deemed acceptable. The aforementioned results indicate that B-PCHS possesses satisfactory stability in catalytic performance, which may be attributed to its chemical stability (the doped B atoms in the final structure) as well as its structural stability (the maintenance of the mesoporous hollow spheres structure during the electrode process).

## Conclusions

In this study, B-PCHS was prepared, and its catalytic performance for the 2e-ORR was investigated. The PCHSs were prepared using SiO<sub>2</sub> particles as a hard template, and the B elements were doped into the carbon skeleton as the form of B-C bonds borate transesterification before graphitization. When using B-PCHS as a cathodic catalyst in an alkali electrolyte, the catalytic selectivity for 2e-ORR was above 90% in the range of 0.4–0.7 V<sub>RHE</sub>, and the electrolysis tests for H<sub>2</sub>O<sub>2</sub> generation indicated a generation rate of 902.48 mmol h<sup>-1</sup> g<sub>cat</sub><sup>-1</sup> at 0.4 V<sub>RHE</sub> with a current density of 59.13 mA cm<sup>-2</sup>. By conducting a contrastive analysis using PCHS and pre-B-PCHS as the comparison samples, it is clarified that the catalytic activity of B-PCHS is attributed to the structure of porous hollow spheres, which facilitates mass transfer during the ORR process, and the catalytic selectivity of B-PCHS originates from the doped B elements. It is noticeable that only the B atoms with a moderate concentration facilitate the 2e-ORR pathway. Finally, the chemical stability of B-C bonds and the structural stability of mesopores in B-PCHS guarantee the durability of its catalytic performance for H<sub>2</sub>O<sub>2</sub> generation.

## Limitations of the study

There was a lack of clear evidence for the mechanism of the effect of B-element doping on the morphology of the products during the preparation process. The existence form and chemical structure of B atoms in the catalysts were not clear. The gas diffusion electrode (GDE), which can break through the limitation of oxygen solubility and effectively promote oxygen reduction kinetics, is a need for practical applications but was not used in this study. In the future, this is an important research direction for us.

## STAR★METHODS

Detailed methods are provided in the online version of this paper and include the following:

- KEY RESOURCES TABLE
- RESOURCE AVAILABILITY
  - Lead contact
  - Materials availability
  - Data and code availability
- METHOD DETAILS
  - Materials and chemicals
  - Synthesis of boron-doped porous carbon hollow spheres
  - Synthesis of pre-B-PCHS
  - Synthesis of PCHS
  - Characterizations
  - Electrochemical testing
  - Continuous electrolysis for H<sub>2</sub>O<sub>2</sub> generation
  - DFT calculations

## SUPPLEMENTAL INFORMATION

Supplemental information can be found online at <https://doi.org/10.1016/j.isci.2024.109553>.

## ACKNOWLEDGMENTS

This project was supported by the National Natural Science Foundation of China (no. 22075012).

## AUTHOR CONTRIBUTIONS

Z.S., Z.W., and Y.C. conceived the project and designed the experiments. Y.C. supervised the project. Z.S., K.L., and K.F. conducted the experimental measurements. H. Jiang conducted the DFT calculations. H. Jin and A.L. helped conduct the structural characterizations. Z.S., Z.W., Y.T., Y.S., P.W., and Y.C. wrote the manuscript with support from all authors.

## DECLARATION OF INTERESTS

The authors declare no competing interests.

Received: February 8, 2024

Revised: March 6, 2024

Accepted: March 21, 2024

Published: March 23, 2024

## REFERENCES

1. Siahrostami, S., Villegas, S.J., Bagherzadeh Mostaghimi, A.H., Back, S., Farimani, A.B., Wang, H., Persson, K.A., and Montoya, J. (2020). A Review on Challenges and Successes in Atomic-Scale Design of Catalysts for Electrochemical Synthesis of Hydrogen Peroxide. *ACS Catal.* **10**, 7495–7511. <https://doi.org/10.1021/acscatal.0c01641>.
2. Lim, J.S., Sa, Y.J., and Joo, S.H. (2022). Catalyst design, measurement guidelines, and device integration for H<sub>2</sub>O<sub>2</sub> electrosynthesis from oxygen reduction. *Cell Rep. Phys. Sci.* **3**, 100987. <https://doi.org/10.1016/j.xcrp.2022.100987>.
3. Melchionna, M., Fornasiero, P., and Prato, M. (2019). The Rise of Hydrogen Peroxide as the Main Product by Metal-Free Catalysis in Oxygen Reductions. *Adv. Mater.* **31**, 1802920. <https://doi.org/10.1002/adma.201802920>.
4. Lazaridis, T., Stühmeier, B.M., Gasteiger, H.A., and El-Sayed, H.A. (2022). Capabilities and limitations of rotating disk electrodes versus membrane electrode assemblies in the investigation of electrocatalysts. *Nat. Catal.* **5**, 363–373. <https://doi.org/10.1038/s41929-022-00776-5>.
5. Byeon, A., Yun, W.C., Kim, J.M., and Lee, J.W. (2023). Recent progress in heteroatom-doped carbon electrocatalysts for the two-electron oxygen reduction reaction. *Chem. Eng. J.* **456**, 141042. <https://doi.org/10.1016/j.cej.2022.141042>.
6. Lu, Z., Chen, G., Siahrostami, S., Chen, Z., Liu, K., Xie, J., Liao, L., Wu, T., Lin, D., Liu, Y., et al. (2018). High-efficiency oxygen reduction to hydrogen peroxide catalyzed by oxidized carbon materials. *Nat. Catal.* **1**, 156–162. <https://doi.org/10.1038/s41929-017-0017-x>.
7. Kulkarni, A., Siahrostami, S., Patel, A., and Nørskov, J.K. (2018). Understanding Catalytic Activity Trends in the Oxygen Reduction Reaction. *Chem. Rev.* **118**, 2302–2312. <https://doi.org/10.1021/acs.chemrev.7b00488>.
8. Siahrostami, S., Verdaguer-Casadevall, A., Karamad, M., Deiana, D., Malacrida, P., Wickman, B., Escudero-Escribano, M., Paoli, E.A., Frydendal, R., Hansen, T.W., et al. (2013). Enabling direct H<sub>2</sub>O<sub>2</sub> production through rational electrocatalyst design. *Nat. Mater.* **12**, 1137–1143. <https://doi.org/10.1038/nmat3795>.
9. Cao, P., Quan, X., Nie, X., Zhao, K., Liu, Y., Chen, S., Yu, H., and Chen, J.G. (2023). Metal single-site catalyst design for electrocatalytic production of hydrogen peroxide at industrial-relevant currents. *Nat. Commun.* **14**, 172. <https://doi.org/10.1038/s41467-023-35839-z>.
10. Verdaguer-Casadevall, A., Deiana, D., Karamad, M., Siahrostami, S., Malacrida, P., Hansen, T.W., Rossmeisl, J., Chorkendorff, I., and Stephens, I.E.L. (2014). Trends in the Electrochemical Synthesis of H<sub>2</sub>O<sub>2</sub>: Enhancing Activity and Selectivity by Electrocatalytic Site Engineering. *Nano Lett.* **14**, 1603–1608. <https://doi.org/10.1021/nl500037x>.
11. Hu, J., Shang, W., Xin, C., Guo, J., Cheng, X., Zhang, S., Song, S., Liu, W., Ju, F., Hou, J., and Shi, Y. (2023). Uncovering Dynamic Edge-Sites in Atomic Co-N-C Electrocatalyst for Selective Hydrogen Peroxide Production. *Angew. Chem. Int. Ed.* **62**, e202304754. <https://doi.org/10.1002/anie.202304754>.
12. Chen, S., Luo, T., Li, X., Chen, K., Fu, J., Liu, K., Cai, C., Wang, Q., Li, H., Chen, Y., et al. (2022). Identification of the Highly Active Co–N<sub>4</sub> Coordination Motif for Selective Oxygen Reduction to Hydrogen Peroxide. *J. Am. Chem. Soc.* **144**, 14505–14516. <https://doi.org/10.1021/jacs.1c11467>.
13. Yan, M., Wei, Z., Gong, Z., Johannessen, B., Ye, G., He, G., Liu, J., Zhao, S., Cui, C., and Fei, H. (2023). Sb<sub>2</sub>S<sub>3</sub>-templated synthesis of sulfur-doped Sb–N–C with hierarchical architecture and high metal loading for H<sub>2</sub>O<sub>2</sub> electrosynthesis. *Nat. Commun.* **14**, 368. <https://doi.org/10.1038/s41467-023-36078-y>.
14. Zhang, Y., Wang, M., Zhu, W., Fang, M., Ma, M., Liao, F., Yang, H., Cheng, T., Pao, C.-W., Chang, Y.-C., et al. (2023). Metastable Hexagonal Phase SnO<sub>2</sub> Nanoribbons with Active Edge Sites for Efficient Hydrogen Peroxide Electrolysis in Neutral Media. *Angew. Chem. Int. Ed.* **62**, e202218924. <https://doi.org/10.1002/anie.202218924>.
15. Ross, R.D., Sheng, H., Ding, Y., Janes, A.N., Feng, D., Schmidt, J.R., Segre, C.U., and Jin, S. (2022). Operando Elucidation of Electrocatalytic and Redox Mechanisms on a 2D Metal Organic Framework Catalyst for Efficient Electrosynthesis of Hydrogen Peroxide in Neutral Media. *J. Am. Chem. Soc.* **144**, 15845–15854. <https://doi.org/10.1021/jacs.2c06810>.
16. Dan, M., Zhong, R., Hu, S., Wu, H., Zhou, Y., and Liu, Z.-Q. (2022). Strategies and challenges on selective electrochemical hydrogen peroxide production: Catalyst and reaction medium design. *Chem Catal.* **2**, 1919–1960. <https://doi.org/10.1016/j.cheecat.2022.06.002>.
17. Xia, Y., Zhao, X., Xia, C., Wu, Z.-Y., Zhu, P., Kim, J.Y.T., Bai, X., Gao, G., Hu, Y., Zhong, J., et al. (2021). Highly active and selective oxygen reduction to H<sub>2</sub>O<sub>2</sub> on boron-doped carbon for high production rates. *Nat. Commun.* **12**, 4225. <https://doi.org/10.1038/s41467-021-24329-9>.
18. Liu, L., Kang, L., Chutia, A., Feng, J., Michalska, M., Ferrer, P., Grinter, D.C., Held, G., Tan, Y., Zhao, F., et al. (2023). Spectroscopic Identification of Active Sites of Oxygen-Doped Carbon for Selective Oxygen Reduction to Hydrogen Peroxide. *Angew. Chem. Int. Ed.* **62**, e202303525. <https://doi.org/10.1002/anie.202303525>.
19. Wu, F., Nan, J., Wang, T., Ge, Z., Liu, B., Chen, M., and Ye, X. (2023). Highly selective electrosynthesis of H<sub>2</sub>O<sub>2</sub> by N, O co-doped graphite nanosheets for efficient electro-Fenton degradation of p-nitrophenol. *J. Hazard Mater.* **446**, 130733. <https://doi.org/10.1016/j.jhazmat.2023.130733>.
20. Xiang, F., Zhao, X., Yang, J., Li, N., Gong, W., Liu, Y., Burguete-Lopez, A., Li, Y., Niu, X., and Fratolocchi, A. (2023). Enhanced Selectivity in the Electroproduction of H<sub>2</sub>O<sub>2</sub> via F/S Dual-Doping in Metal-Free Nanofibers. *Adv. Mater.* **35**, 2208533. <https://doi.org/10.1002/adma.202208533>.
21. Kim, H.W., Bukas, V.J., Park, H., Park, S., Diederichsen, K.M., Lim, J., Cho, Y.H., Kim, J., Kim, W., Han, T.H., et al. (2020). Mechanisms of Two-Electron and Four-Electron Electrochemical Oxygen Reduction Reactions at Nitrogen-Doped Reduced Graphene Oxide. *ACS Catal.* **10**, 852–863. <https://doi.org/10.1021/acscatal.9b04106>.
22. Chang, Y., Li, J., Ma, J., Liu, Y., Xing, R., Wang, Y., and Zhang, G. (2022). Oxygenated boron-doped carbon via polymer dehalogenation as an electrocatalyst for high-efficiency O<sub>2</sub> reduction to H<sub>2</sub>O<sub>2</sub>. *Sci. China Mater.* **65**, 1276–1284. <https://doi.org/10.1007/s40843-021-1891-2>.
23. Byeon, A., Choi, J.W., Lee, H.W., Yun, W.C., Zhang, W., Hwang, C.-K., Lee, S.Y., Han, S.S., Kim, J.M., and Lee, J.W. (2023). CO<sub>2</sub>-derived edge-boron-doped hierarchical porous carbon catalysts for highly effective electrochemical H<sub>2</sub>O<sub>2</sub> production. *Appl. Catal. B Environ.* **329**, 122557. <https://doi.org/10.1016/j.apcatb.2023.122557>.
24. Chen, S., Chen, Z., Siahrostami, S., Higgins, D., Nordlund, D., Sokaras, D., Kim, T.R., Liu, Y., Yan, X., Nilsson, E., et al. (2018). Designing Boron Nitride Islands in Carbon Materials for Efficient Electrochemical Synthesis of Hydrogen Peroxide. *J. Am. Chem. Soc.* **140**, 7851–7859. <https://doi.org/10.1021/jacs.8b02798>.
25. Yuan, Q., Fan, M., Zhao, Y., Wu, J., Raj, J., Wang, Z., Wang, A., Sun, H., Xu, X., Wu, Y., et al. (2023). Facile fabrication of carbon dots containing abundant h-BN/graphite heterostructures as efficient electrocatalyst for hydrogen peroxide synthesis. *Appl. Catal. B Environ.* **324**, 122195. <https://doi.org/10.1016/j.apcatb.2022.122195>.
26. Zhang, H., Noonan, O., Huang, X., Yang, Y., Xu, C., Zhou, L., and Yu, C. (2016). Surfactant-Free Assembly of Mesoporous Carbon Hollow Spheres with Large Tunable Pore Sizes. *ACS Nano* **10**, 4579–4586. <https://doi.org/10.1021/acsnano.6b00723>.
27. Wang, J., Yang, C., Wang, J., Han, L., and Wei, M. (2019). Two-dimensional MoN@N-doped carbon hollow spheres as an anode material for high performance lithium-ion battery. *Electrochim. Acta* **295**, 246–252. <https://doi.org/10.1016/j.electacta.2018.10.159>.
28. Zhu, X., Tan, X., Wu, K.-H., Chiang, C.-L., Lin, Y.-C., Lin, Y.-G., Wang, D.-W., Smith, S., Lu, X., and Amal, R. (2019). N,P co-coordinated Fe species embedded in carbon hollow spheres for oxygen electrocatalysis. *J. Mater. Chem. A* **7**, 14732–14742. <https://doi.org/10.1039/C9TA03011E>.
29. Pang, Y., Wang, K., Xie, H., Sun, Y., Titirici, M.-M., and Chai, G.-L. (2020). Mesoporous Carbon Hollow Spheres as Efficient Electrocatalysts for Oxygen Reduction to Hydrogen Peroxide in Neutral Electrolytes.

- ACS Catal. 10, 7434–7442. <https://doi.org/10.1021/acscatal.0c00584>.
30. Gao, J., Liu, Y., and Wang, F. (2001). Structure and properties of boron-containing bisphenol-A formaldehyde resin. *Eur. Polym. J.* 37, 207–210. [https://doi.org/10.1016/S0014-3057\(00\)00095-1](https://doi.org/10.1016/S0014-3057(00)00095-1).
  31. Li, S., Pasc, A., Fierro, V., and Celzard, A. (2016). Hollow carbon spheres, synthesis and applications – a review. *J. Mater. Chem. A* 4, 12686–12713. <https://doi.org/10.1039/C6TA03802F>.
  32. Lin, R., Kang, L., Lisowska, K., He, W., Zhao, S., Hayama, S., Hutchings, G.J., Brett, D.J.L., Corà, F., Parkin, I.P., and He, G. (2023). Approaching Theoretical Performances of Electrocatalytic Hydrogen Peroxide Generation by Cobalt-Nitrogen Moieties. *Angew. Chem. Int. Ed.* 62, e202301433. <https://doi.org/10.1002/anie.202301433>.
  33. Li, Y., Chen, J., Ji, Y., Zhao, Z., Cui, W., Sang, X., Cheng, Y., Yang, B., Li, Z., Zhang, Q., et al. (2023). Single-atom Iron Catalyst with Biomimetic Active Center to Accelerate Proton Spillover for Medical-level Electrosynthesis of H<sub>2</sub>O<sub>2</sub> Disinfectant. *Angew. Chem. Int. Ed.* 62, e202306491. <https://doi.org/10.1002/anie.202306491>.
  34. Fan, W., Duan, Z., Liu, W., Mehmood, R., Qu, J., Cao, Y., Guo, X., Zhong, J., and Zhang, F. (2023). Rational design of heterogenized molecular phthalocyanine hybrid single-atom electrocatalyst towards two-electron oxygen reduction. *Nat. Commun.* 14, 1426. <https://doi.org/10.1038/s41467-023-37066-y>.
  35. Fu, H., Zhang, N., Lai, F., Zhang, L., Wu, Z., Li, H., Zhu, H., and Liu, T. (2022). Lattice Strained B-Doped Ni Nanoparticles for Efficient Electrochemical H<sub>2</sub>O<sub>2</sub> Synthesis. *Small* 18, 2203510. <https://doi.org/10.1002/smll.202203510>.
  36. An, S., Li, X., Shang, S., Xu, T., Yang, S., Cui, C.X., Peng, C., Liu, H., Xu, Q., Jiang, Z., and Hu, J. (2023). One-Dimensional Covalent Organic Frameworks for the 2e<sup>-</sup> Oxygen Reduction Reaction. *Angew. Chem. Int. Ed.* 62, e202218742. <https://doi.org/10.1002/anie.202218742>.
  37. Zhang, C., Wu, C., Wang, L., and Liu, G. (2023). Selective H<sub>2</sub>O<sub>2</sub> Electrosynthesis over Defective Carbon from Electrochemical Etching of Molybdenum Carbide. *ACS Appl. Mater. Interfaces* 15, 838–847. <https://doi.org/10.1021/acscami.2c15467>.
  38. Kim, M., Firestein, K.L., Fernando, J.F.S., Xu, X., Lim, H., Golberg, D.V., Na, J., Kim, J., Nara, H., Tang, J., and Yamauchi, Y. (2022). Strategic design of Fe and N co-doped hierarchically porous carbon as superior ORR catalyst: from the perspective of nanoarchitectonics. *Chem. Sci.* 13, 10836–10845. <https://doi.org/10.1039/D2SC02726G>.

## STAR★METHODS

## KEY RESOURCES TABLE

REAGENT or RESOURCE	SOURCE	IDENTIFIER
Chemicals, peptides, and recombinant proteins		
Tetraethyl silicate	Shanghai Aladdin Biochemical Technology Co., Ltd	98%
Tetrapropyl silicate	Shanghai Aladdin	97%
resorcinol	Shanghai Aladdin	97%
HF solution	Shanghai Aladdin	5%
Nafion solution	DuPont de Nemours, Inc.	5%
Oxygen	Beijing Hairui Tongda Gas Technology Co.	99.99%
Argon	Beijing Hairui Tongda	99.99%
Other		
Scanning Electron Microscope (SEM)	Carl Zeiss AG	Zeiss supra 55
Transmission Electron Microscope (TEM)	FEI Company	Tecnai G2F30
X-ray Photoelectron Spectroscopy (XPS)	Thermo Scientific	K-Alpha
Raman Spectrometer (Raman)	Horiba Semiconductor	LabRAM HR Evolution
Specific surface area and porosity analyser (BET)	Micromeritics	ASAP 2460
Inductively coupled plasma-optical emission spectrometry (ICP-OES)	Agilent	725ES
Electrochemical workstation	Shanghai Chenhua	CHI760E
Modulated Speed Rotator (MSR)	Pine Research	MSR

## RESOURCE AVAILABILITY

## Lead contact

Further information and requests for data should be directed and will be fulfilled by the lead contact, Prof./Dr. Yongmei Chen ([chenym@buct.edu.cn](mailto:chenym@buct.edu.cn)).

## Materials availability

All materials generated in this study are available from the [lead contact](#) without restriction.

## Data and code availability

- All data reported in this paper will be shared by the [lead contact](#) upon request.
- This paper does not report original code.
- Any additional information required to reanalyze the data reported in this paper is available from the [lead contact](#) upon request.

## METHOD DETAILS

## Materials and chemicals

Tetraethyl silicate (Aladdin, 98%), tetrapropyl silicate (Aladdin, 97%), resorcinol (Aladdin, 97%), HF solution (Aladdin, 5%), and Nafion solution (DuPont, 5%) were used as received. The other chemicals were obtained from the Beijing Chemical Plant without any further treatment.

## Synthesis of boron-doped porous carbon hollow spheres

280  $\mu$ L tetraethyl silicate (1.2 mmol) and 3.15 mL tetrapropyl silicate (10.8 mmol) were sequentially added to a mixture of 70 mL ethanol, 10 mL deionized water, and 2.15 mL 35 wt % ammonia under continuous stirring to facilitate the slow hydrolysis of silicates and the formation of SiO<sub>2</sub> particles. About 15 min later, 0.4 g resorcinol (3.64 mmol) and 0.56 mL 37% formaldehyde (7.46 mmol) aqueous solution were added to the above system. The reaction was then continued for 12 h under stirring.<sup>29</sup> Subsequently, a catalytic amount of KOH (~50 mg) and a borate ester solution, prepared by dissolving 223.3 mg H<sub>3</sub>BO<sub>3</sub> (3.6 mmol) in 1315  $\mu$ L methanol, was added to the above reaction solution. The mixture was stirred for an additional 12 h to complete the transesterification process. A yellowish precipitate formed in the reaction system, and the solid

was separated by centrifugation, washed several times with deionized water and ethanol, and then dried in a vacuum oven at 60°C overnight. A yellowish solid powder was obtained, which might be boron-doped phenolic resin-coated silica spheres. In the next step, it was placed in a Al<sub>2</sub>O<sub>3</sub> crucible in a tube furnace and heated to 900°C for 5 h at a heating rate of 5 °C min<sup>-1</sup> under Ar atmosphere (50 mL min<sup>-1</sup>). Subsequently, it was naturally cooled to room temperature, resulting in the formation of a black powder consisting of boron-doped carbon-coated silica spheres. Finally, the SiO<sub>2</sub> in the samples was etched off using a 5 wt % HF solution, and then B-PCHS were obtained after washing and drying.

### Synthesis of pre-B-PCHS

The dosage of each reactant and the operating conditions for pre-B-PCHS synthesis was the same as the procedure of B-PCHS described above, with the exception that dimethyl (3-hydroxyphenyl) boronate was used instead of resorcinol. The formation reaction of dimethyl (3-hydroxyphenyl) boronate and its polycondensation reaction with formaldehyde is shown in the [Scheme S1](#). The whole procedure for synthesis of pre-B-PCHS is following.

A catalytic amount of KOH (~50 mg) was added to 0.4 g resorcinol and then mixed with the borate ester solution which was obtained by dissolving 223.3 mg H<sub>3</sub>BO<sub>3</sub> (3.6 mmol) in 1315 μL methanol and stirred for 12 h. Obtaining dimethyl (3-hydroxyphenyl) boronate as a transparent viscous yellowish liquid. 280 μL tetraethyl silicate (1.2 mmol) and 3.15 mL tetrapropyl silicate (10.8 mmol) were sequentially added into a mixture solution of 70 mL ethanol, 10 mL deionized water and 2.15 mL 35 wt % ammonia under continuous stirring to facilitate slow hydrolysis of silicates and form SiO<sub>2</sub> particles. 15 min later, the obtained dimethyl (3-hydroxyphenyl) boronate and 0.56 mL 37% formaldehyde (7.46 mmol) aqueous solution were added to the above system. The reaction was then continued for 24 h under stirring. After the same separation, calcination, and etching processes, the pre-B-PCHS were obtained.

### Synthesis of PCHS

The synthesis of PCHS follows the ref. 1 and the details are described as following.

280 μL tetraethyl silicate (1.2 mmol) and 3.15 mL tetrapropyl silicate (10.8 mmol) were sequentially added into a mixture solution of 70 mL ethanol, 10 mL deionized water and 2.15 mL 35 wt % ammonia under continuous stirring to facilitate slow hydrolysis of silicates and form SiO<sub>2</sub> particles. 15 min later, 0.4 g resorcinol (3.64 mmol) and 0.56 mL 37% formaldehyde (7.46 mmol) aqueous solution were added to the above system. The reaction was then continued for 24 h under stirring. the same separation, calcination, and etching processes, PCHS were obtained after washing and drying.

### Characterizations

The scanning electron microscopy images were obtained using a field emission scanning electron microscope (Zeiss supra 55). The transmission electron microscopy (TEM) images were obtained using FEI Tecnai G2F30 at 300kV. X-ray photoelectron spectroscopy (XPS) data were obtained using a Thermo Scientific K-Alpha instrument with an Al K $\alpha$  X-ray source, and the peak areas were fitted using the software XPSPEAK41 by Lorentz (30%) and Gaussian (70%) functions until a fitting criterion of  $\chi^2$  less than 10. The content of elements was measured after samples underwent microwave digestion, followed by ICP-OES testing, which was conducted using an Agilent 725ES and an Agilent 5110 (OES). The N<sub>2</sub> adsorption and desorption isotherms were characterized at 77 K using the Micromeritics ASAP 2460. Horiba LabRAM HR Evolution tested the Raman spectra with a 532 nm wavelength laser, and the I<sub>D</sub>/I<sub>G</sub> ratio was calculated based on the peak-to-height ratio.

### Electrochemical testing

The typical electrochemical study was performed at a CHI760E electrochemical workstation (Shanghai Chenhua) in a standard three-electrode system, in which a platinum plate served as the counter electrode, and a saturated calomel electrode (SCE) connected by a salt bridge served as the reference electrode. Notably, all potentials mentioned in this study have been converted to compare with the Reversible Hydrogen Electrode (RHE) using [Equation 1](#).

$$E_{\text{RHE}} = E_{\text{SCE}} + 0.2438 + 0.0592 \times \text{pH} \quad (\text{Equation 1})$$

A ring-disk electrode, which consists of a glassy carbon disk (0.2475 cm<sup>2</sup>) and a Pt ring (0.1866 cm<sup>2</sup>), served as the working electrode. The catalyst ink was prepared by dispersing 2 mg catalyst in a mixture consisting of 700 μL isopropanol, 300 μL water, and 20 μL 5% Nafion, followed by sonication for 30 min 8 μL of the ink was loaded onto the surface of disk electrode, and the final catalyst loading was 0.063 mg cm<sup>-2</sup>.

Cyclic voltammetry measurement was performed in 1 mol L<sup>-1</sup> KOH solution under Ar or O<sub>2</sub> atmosphere in the range of 0.1 V–1.2 V with a scanning rate of 50 mV s<sup>-1</sup>.

The CV curves in the non-Faraday region were respectively recorded with scanning rates of 5, 10, 25, 50, 100, 200 and 400 mV s<sup>-1</sup>, and the difference in current density with the current density at open circuit potential, was taken to fit to the scan rate to determine the bilayer capacitance, C<sub>dl</sub>, of the material.

Linear sweep voltammetry was conducted with rotation controlled by an MSR electrode-rotating controller (PINE). To ensure the cleanliness on ring electrode prior to each electrochemical measurement, the RRDE is performed CV tests for 1000 cycles in 1 mol L<sup>-1</sup> H<sub>2</sub>SO<sub>4</sub> at a sweep rate of 100 mV s<sup>-1</sup> on the ring in the range of –1.0 to 2.0 V, followed by the ring electrode is subjected to the chronoamperometry method with a constant potential of 0.5 V for 60 s to reduce the potentially present PtO<sub>x</sub>. In addition, the reference electrodes (saturated calomel electrode) are calibrated to 0.2438 V before testing. As to evaluate the catalytic selectivity for 2e-ORR, the potential on disk was

scanned from 1.0 V to 0.1 V in rate of  $5 \text{ mV s}^{-1}$ , and the ring potential was kept at 1.2 V with the rotating rate of 1600 rpm to detect  $\text{H}_2\text{O}_2$  generated on the disk, and the catalytic selectivity of  $\text{H}_2\text{O}_2$  was calculated as described in Equation 2. The transferred electron number ( $n$ ) during the ORR reaction was calculated using Equation 3.

$$\text{H}_2\text{O}_2\% = 200 \times \frac{I_{\text{ring}}/N_{\text{test}}}{I_{\text{disk}} + I_{\text{ring}}/N_{\text{test}}} \quad (\text{Equation 2})$$

$$n = 4 \times \frac{I_{\text{disk}}}{I_{\text{disk}} + I_{\text{ring}}/N_{\text{test}}} \quad (\text{Equation 3})$$

where  $I_{\text{ring}}$ ,  $I_{\text{disk}}$  represent the ring current, disk current (both currents have deducted the background), respectively. The  $N_{\text{test}}$  represents the collection efficiency of the catalyst-loaded RRDE, which was determined using  $\text{K}_3[\text{Fe}(\text{CN})_6]$  after each LSV test. The theoretical  $N$  value was 0.37.

The transferring electron number during the ORR reaction was also calculated using the Koutechy-Levich equation. The LSV curves were respectively tested at 400, 625, 900, 1225, 1600, 2025, and 2500 rpm. The current density corresponding to the half-wave potential was fitted to the rotational speed in radians after applying the transformation (Equation 4). The obtained slope was then substituted into Equation 5 for calculation in order to determine the number of electrons transferred during the ORR process.

$$\frac{1}{j} = \frac{1}{j_D} + \frac{1}{j_K} = \frac{1}{K\omega^{1/2}} + \frac{1}{j_K} \quad (\text{Equation 4})$$

$$K = 0.0620nFD_i^{2/3}\nu^{-1/6}c_i^0 \quad (\text{Equation 5})$$

Where  $j$ ,  $j_D$ , and  $j_K$  represent the current densities at the experimentally measured half-wave potentials, the limiting diffusion current density, and the kinetic control current density, respectively.  $\omega$  represents the rotational speed of the electrodes,  $n$  denotes the number of electrons transferred during the ORR process,  $F$  stands for Faraday's constant ( $96485 \text{ C mol}^{-1}$ ),  $D_i$  represents the diffusion rate of oxygen ( $1.65 \times 10^{-5} \text{ cm}^2 \text{ s}^{-1}$ ),  $\nu$  stands for the solution's kinetic viscosity ( $1 \text{ mol L}^{-1} \text{ KOH}$ :  $0.01 \text{ cm}^2 \text{ s}^{-1}$ ), and  $c_i^0$  denotes the concentration of oxygen in solution ( $0.84 \times 10^{-3} \text{ mol cm}^{-3}$ ).

The electrochemical impedance spectroscopy (EIS) was tested in the same three-electrode system with RRDE tests. After initial activation of working electrode, EIS was recorded at the corresponding half-wave potential of each catalyst with working electrode rotating at 1600 rpm and immersed in  $\text{O}_2$ -saturated  $0.1 \text{ mol L}^{-1} \text{ KOH}$ . The EIS results were fitted according to the following  $R_e(Q(R_{ct}O))$  equivalent circuit. Where  $R_e$  represents the solution resistance between the reference and working electrodes;  $Q$  represents the constant phase angle element, which is used to provide feedback on the capacitance of the electrode interface under inhomogeneous (discrete) conditions;  $R_{ct}$  represents the charge transfer resistance, which is used to assess the magnitude of resistance to the electron transfer process at intermediate frequencies; and  $O$  represents the finite-length diffusion process (or porous-boundary Warburg diffusion), which represents the diffusion of a thin layer of a reactant from a bulk solution through the Nernst diffusion layer (abbreviated NDL). The parameters obtained from fitting was given in Table S1.

The Tafel slopes were calculated from the staircase voltammetry method. The potential scanned from 0.9 to 0.8 V in steps of 1 mV, and each step is held for 30 s. The entire experiment was performed in an oxygen-saturated  $1 \text{ mol L}^{-1} \text{ KOH}$ , and the disk electrode was rotated at 1600 rpm.

For an accelerated durability test, CV was performed in range of 0.2 V–1.0 V at a scan rate of  $200 \text{ mV s}^{-1}$  for 2000 cycles under  $\text{O}_2$ , and the comparison of the CV curves before and after the test was used to evaluate the stability of the catalysts. Moreover, a chronoamperometry stability test was conducted by keeping the disk potential of 0.5 V and the ring potential of 1.2 V for 20 h, and the change in catalytic selectivity for 2e-ORR was evaluated based on the change in the ring current during the test. The sampling rate was set at  $1 \text{ point s}^{-1}$ .

### Continuous electrolysis for $\text{H}_2\text{O}_2$ generation

Electrochemical generation of  $\text{H}_2\text{O}_2$  was conducted in  $1.0 \text{ mol L}^{-1} \text{ KOH}$  solution in an H-type electrolysis bath with a Nafion diaphragm, in which a catalyst-loaded carbon paper was used as the working electrode, a Pt plate as the counter electrode, and an SCE connected to the cathode chamber by a salt bridge as the reference electrode. A cathode electrode was prepared by uniformly spraying the corresponding catalyst ink (the same content as mentioned above) onto carbon paper with a loading of  $1 \text{ mg cm}^{-2}$  using a spray torch. The electrolysis was conducted in a constant current model with  $\text{O}_2$  gas bubbling near the cathode for 20 min. The generated  $\text{H}_2\text{O}_2$  in the electrolyte after electrolysis was determined by  $\text{KMnO}_4$  titration method, and the Faraday efficiency (FE) was calculated following Equation 6.

$$\text{FE}(\%) = \frac{5C_{\text{KMnO}_4}V_{\text{KMnO}_4}}{2V_m} \cdot \frac{2FV_{\text{H}_2\text{O}_2}}{\int_0^t Idt} \cdot 100\% \quad (\text{Equation 6})$$

where  $c_{\text{KMnO}_4}$ ,  $V_{\text{KMnO}_4}$ ,  $m$ ,  $F$ ,  $V_{\text{H}_2\text{O}_2}$ ,  $I$ , and  $t$  respectively represent the concentration and volume of  $\text{KMnO}_4$  used in the titration, the volume of electrolyte measured during the titration, Faraday's constant ( $96485 \text{ C mol}^{-1}$ ), the total volume of electrolyte, the current detected by the chronoamperometry, and the duration of the electrolysis. The generation rate of  $\text{H}_2\text{O}_2$  is calculated following Equation 7.

$$\text{H}_2\text{O}_2 \text{ production rate} = \frac{5c_{\text{KMnO}_4}V_{\text{KMnO}_4}}{2V_m} \cdot \frac{V_{\text{H}_2\text{O}_2}}{m_{\text{cat}}t} \quad (\text{Equation 7})$$

where  $m_{\text{cat}}$  represents the mass of the loaded catalyst on the cathode.

### DFT calculations

All the first-principles calculations are performed via Vienna Ab initio Simulation Package (VASP) with the projector augmented wave (PAW) approach to describe the interaction between core and valence electrons. The exchange-correlation interactions are treated by the generalized gradient approximation Perdew-Burke-Ernzerhof (GGA-PBE). A cut-off energy of 400 eV is used for the plane wave basis set. A  $4 \times 4$  graphene supercell was used as the initial structure. The vacuum thickness of 15 Å is maintained to prevent the interaction between adjacent layers. The DFT-D3 method developed by Grimme is adopted to describe long-range vdW interactions. For structural optimization, the convergence criteria for energy and force set to  $10^{-5}$  eV and 0.02 eV/Å. The Brillouin zone is sampled using Monkhorst-Pack mesh of  $2 \times 2 \times 1$ .